AD-A252 908

92-18836

MASSACHUSETTS INSTITUTE OF TECHNOLOGY
LINCOLN LABORATORY

840-Hz Nd:YAG LASER SOURCE OF SODIUM RESONANCE RADIATION

FINAL REPORT
TO THE
U.S. AIR FORCE PHILLIPS LABORATORY

JANUARY 1989 — MARCH 1991

ISSUED 11 MAY 1992

Approved for public release; distribution is unlimited.

LEXINGTON   MASSACHUSETTS

ABSTRACT

A 20-W average power laser source of sodium resonance radiation has been developed and delivered to the Air Force Phillips Laboratory to generate a fluorescence spot in the earth's mesospheric sodium layer for atmospheric adaptive optics applications. The sodium resonance radiation was generated by sum-frequency mixing 1.06- and 1.32-μm Nd:YAG laser radiation in a lithium triborate crystal. The pulsed Nd:YAG lasers operated with a repetition rate of 840 Hz and pulse lengths of about 100 μs. Sum radiation was resonant with the sodium D_2 transition and generated with an average mixing efficiency of 30%. The lasers were mode-locked with a controlled pulse width that provided a spectrally broadened output that was matched to the 3-GHz Doppler-broadened absorption width of mesospheric sodium.

DTIC QUALITY INSPECTED 3

Accession For	
NTIS GRA&I	☑
DTIC TAB	☐
Unannounced	☐
Justification	
By	
Distribution/	
Availability Codes	
Dist	Avail and/or Special
A-1	

iii

TABLE OF CONTENTS

v

LIST OF ILLUSTRATIONS

vii

LIST OF ILLUSTRATIONS (Continued)

1. INTRODUCTION

A source of sodium resonance radiation capable of generating 24 mJ of energy per 100-μs pulse at a repetition rate of 840 Hz has been developed based on sum-frequency mixing of Nd:YAG laser radiation. The sodium resonance radiation is generated by a laser system that is composed of two individual flashlamp-pumped lasers, one operating at 1.06 μm and the other at 1.32 μm. The peak output intensity of these lasers, even after being mode-locked, is relatively low ($\approx$0.6 MW/cm^2) and, therefore, efficient sum-frequency generation requires significant focusing of the laser radiation into the nonlinear crystal. Lithium triborate (LiB$_3$O$_5$) was found to be the only nonlinear crystal capable of withstanding the very high fluence at the focus and at the same time efficiently mixing the Nd:YAG laser radiation. The high average pump power at which the laser system is operated places a severe thermal load on the Nd:YAG rods and results in strong, thermally induced lensing and birefringence. The laser oscillators, and to a lesser extent the amplifiers, are very sensitive to changes in the level of thermal loading. Small variations in this thermal loading, resulting from aging of the flashlamps or variation in the drive current, result in a significant change in the output power and beam quality of the laser oscillators. As a result of this sensitivity it is difficult to maintain the maximum level of sum radiation power. It appears that the system reliably generates about 14 mJ per pulse, while generating 24 mJ per pulse requires significant effort.

The manufacturer, Continuum, Inc., delivered the laser system shown in Figure 1 to MIT Lincoln Laboratory in October 1989, after an unexpected seven-month delay that was caused by a difficulty in meeting the original specifications and a military priority imposed by Lockheed that forced Continuum to temporarily stop work on the system. Because the laser system did not meet the original specifications when delivered to Lincoln, much unanticipated work was required. It was necessary to restrict oscillation to the TEM$_{00}$ mode without reducing output power and to obtain as much gain in the amplifiers as possible without degrading laser beam quality. In addition to installing mode-lockers and intracavity doubling crystals, almost all the original hardware was replaced to allow greater stability and finer control of each optical element. The persistent leakage of water onto the Nd:YAG optical surfaces severely delayed the development of the laser system and finally required Lincoln to develop a new sleeve to hold the Nd:YAG rods and a new type of O-ring to seal the sleeve to the pump housing. Several mixing crystals and geometries were tested before deciding to use noncritically phase-matched LiB$_3$O$_5$. The final laser system as delivered to the Air Force Phillips Laboratory in March 1991 is shown in Figures 2 and 3.

This laser system represents the current state of the art for the production of a high repetition rate, long pulse length source of sodium resonance radiation using commercially available components. Moreover, the development of this laser system has provided much of the knowledge required to design and construct a higher average power source of sodium resonance radiation with minimum risk. A more compact laser system with long-term alignment stability and substantially higher output power can be constructed using 0.808-μm diode laser radiation to pump a Nd:YAG zig-zag slab laser system. Diode laser pumping reduces the thermal load on the Nd:YAG crystal, while the zig-zag slab geometry reduces the adverse effects of thermally induced birefringence and wavefront distortion. In recent years the cost of diode laser arrays has fallen, and a diode-pumped, high repetition rate, high average power, high beam quality Nd:YAG laser system costs less than a similar flashlamp-pumped laser system.

1

137715-1

Figure 1. Initial hardware delivered to MIT Lincoln Laboratory from Continuum, Inc., for the construction of the 840-Hz laser system. Most of the optical mounts shown in this photograph had to be replaced by higher quality mounts.

2

172665-1
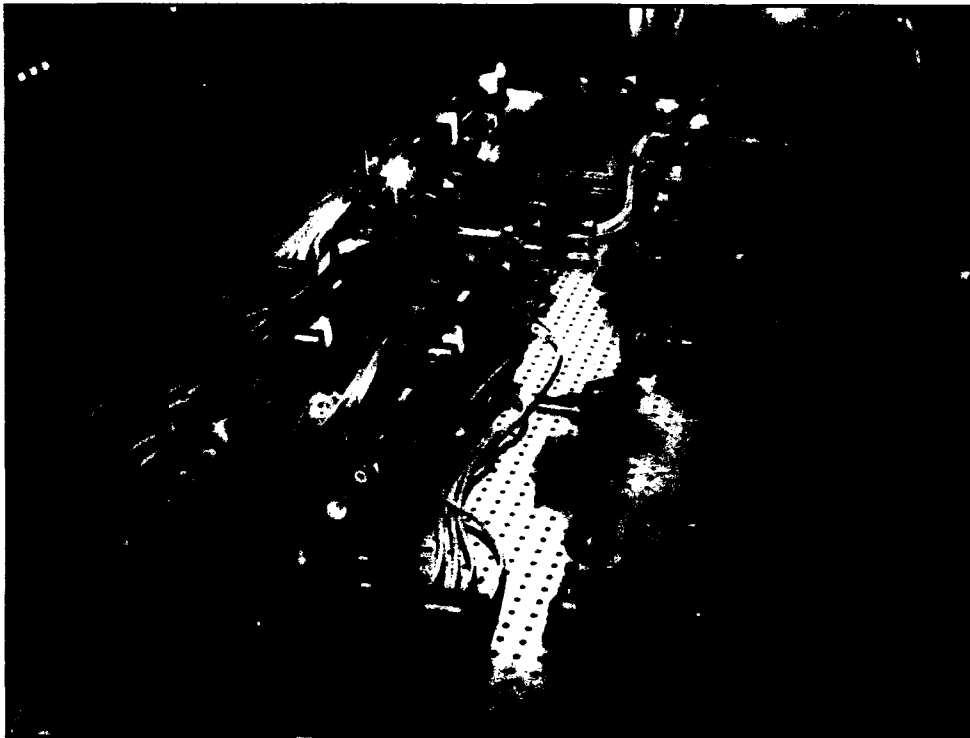
Figure 2. The 840-Hz laser system as delivered to the Air Force Phillips Laboratory in March 1991. Oscillators are in the foreground. The 1.32- and 1.06-μm oscillators are in the extreme left and central left, respectively. The light generated by the intracavity nonlinear crystal can be seen in the lower left. The amplifiers are in the background. The sodium resonance radiation generated in the LiB_3O_5 crystal is evident in the right part of the photograph.

3

Figure 3. The 840-Hz laser system as viewed from the amplifier end of the laser bench. The 1.32- and 1.06-μm amplifiers are in the right and left foregrounds, respectively. The LiB_3O_5 nonlinear crystal is in the upper central background.

2. LASER OSCILLATORS

A schematic of the laser system is shown in Figure 4. The laser oscillators are operated in the stable regime and in the TEM_{00} mode to obtain optimum beam quality for efficient sum-frequency mixing. Each oscillator, to first order, may be considered as a simple cavity with two thick lenses placed symmetrically between two plane parallel mirrors. The lenses are produced by the concave surfaces of the 4-mm diameter, 133-mm-long Nd:YAG rods (which the Laboratory is capable of polishing and coating) and the quadratic index profile that is generated in the rods by the thermal load of the absorbed flashlamp energy. The diameter of the TEM_{00} mode depends on the effective focal length of these lenses, which in turn is inversely proportional to the energy absorbed in the rods [1]. The mode diameter, halfway between the ends of either Nd:YAG rod and as a function of the quadratic index parameter (k), is shown in Figure 5. The quadratic index parameter is proportional to the square root of the energy absorbed in the rods and is defined in the equation describing the variation of the index of refraction $(n(r))$ with the radial distance (r) from the center of the rod: $n(r) = n_0(1 - k^2 r^2/2)$. The plane parallel mirror cavity has two stable regions, 1 and 2 (Figure 5). The mode diameter as a function of position in the cavity for each region is shown in Figure 6. Region 1 corresponds to the upper curve in Figure 6, while region 2 corresponds to the lower curve and exhibits a sharp focus between the two Nd:YAG rods. The laser, as delivered to the Phillips Laboratory, operated in region 1 with lamp powers of about 6 kW. The flashlamps are not rated for the powers needed to operate the cavity in region 2. (Continuum recommended a maximum operating lamp power of 6.3 kW.) The greatest laser power should be obtained by operating the cavity with the greatest mode diameter; however, as the mode diameter is increased, it and the laser power become very sensitive to the pump power. Region 1 extends only over a ± 7% range of pump power, and 1% changes in the pump power can have substantial effects on the laser power. The final 1.06- and 1.32-μm laser oscillator cavities represent a compromise between obtaining high output power and reasonable laser stability.

The performance of the laser oscillators and amplifiers is strongly influenced by the thermally induced birefringence in the Nd:YAG rods [2]. Thermally induced birefringence, if not compensated, depolarizes the output of the laser and consequently lowers the sum-frequency mixing efficiency. The induced birefringence is nonuniform over the cross section of the Nd:YAG rod, varying radially from zero at its thermal center to a maximum at its edge. This birefringence results in variable depolarization of the transmitted laser radiation over the laser beam cross section. In the oscillators this depolarization combines with the intracavity polarizers, resulting in substantial loss of laser power and restricts the laser mode inside the rods to smaller radii than predicted in Figures 5 and 6. In the amplifiers depolarization also results in loss of laser power at the extracavity polarizers and degradation in the transverse beam quality.

The effects of birefringence are minimized by first aligning the laser so that its beam travels through the thermal center of the laser rods, experiencing the least birefringence and operating the laser rods as matched pairs with a 90° polarization rotator between them for birefringence compensation [3,4]. The thermal center of the oscillator rods is found by adjusting the direction of propagation of a polarized HeNe laser beam that is transmitted through the rods while they are being pumped at full operating power until the intensity profile of the HeNe beam (after a crossed polarizer) is that of a symmetric cross. The intracavity aperture that restricted the laser to TEM_{00} operation is then centered on the HeNe beam, and the laser cavity is adjusted to optimize the laser output power without translating this aperture.
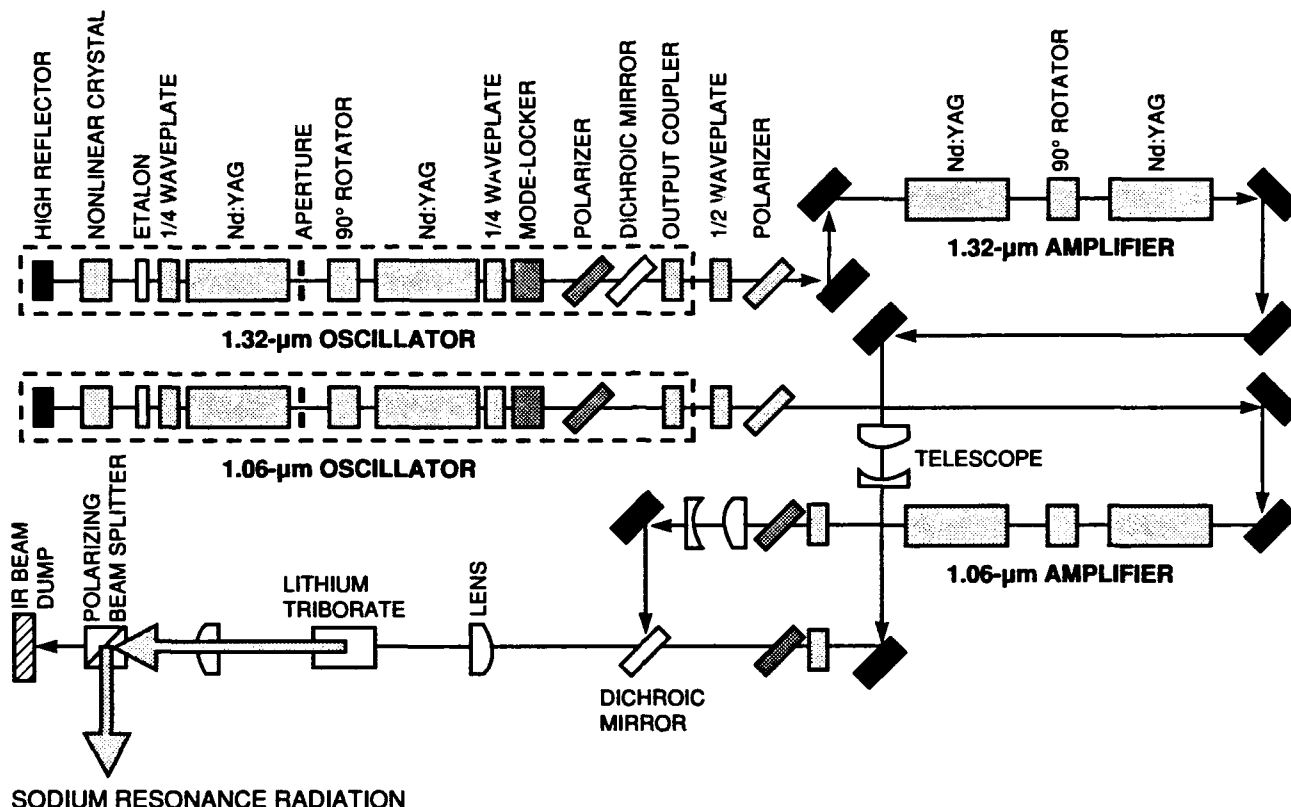
192723-1

1.32-μm OSCILLATOR

HIGH REFLECTOR · NONLINEAR CRYSTAL · ETALON · 1/4 WAVEPLATE · Nd:YAG · APERTURE · 90° ROTATOR · Nd:YAG · 1/4 WAVEPLATE · MODE-LOCKER · POLARIZER · DICHROIC MIRROR · OUTPUT COUPLER · 1/2 WAVEPLATE · POLARIZER

Nd:YAG · 90° ROTATOR · Nd:YAG

1.32-μm AMPLIFIER

1.06-μm OSCILLATOR

TELESCOPE

1.06-μm AMPLIFIER

IR BEAM DUMP · POLARIZING BEAM SPLITTER · LITHIUM TRIBORATE · LENS

DICHROIC MIRROR

SODIUM RESONANCE RADIATION

Figure 4. Schematic of the 1.06- and 1.32-μm, 840-Hz Nd:YAG laser system for sum-frequency mixing in lithium triborate (LiB$_3$O$_5$). Each ≈1.5-m-long oscillator consists of a ≈ 50% output coupler, two flashlamp-pumped Nd:YAG rods, a 90° polarization rotator between the rods for birefringence compensation, a dielectric polarizer (1.06 μm) or Brewster plate (1.32 μm) for laser polarization, a 1/4 waveplate on either side of the laser rods, a nonlinear crystal for spike suppression (1-cm-long antireflection-coated LiIO$_3$ crystal for the 1.32-μm laser and a 0.5-cm-long antireflection-coated KTP crystal for the 1.06-μm laser), an acousto-optic mode locker, a solid etalon for wavelength tuning, and a 100% reflector (flat for the 1.06-μm laser, a −2-m radius of curvature for the 1.32-μm laser). An intracavity aperture restricted laser oscillation to the TEM$_{00}$ cavity mode for both Nd:YAG lasers. The 1.32-μm laser cavity contained a dichroic mirror (transmission at 1.32 μm and reflection at 1.06 μm) for the suppression of 1.06-μm parasitic laser oscillation. A single-frequency source drove both acousto-optic mode lockers, which phase-locked the micropulses for both laser oscillators. The relative phase of the mode-locker drive signals was adjusted to ensure that the micropulses from the 1.06-μm and the 1.32-μm lasers arrived in the sum-frequency mixing crystal at the same time. The output of each oscillator was passed through an amplifier and a telescope to match the beam sizes in the LiB$_3$O$_5$. The 1.06- and the 1.32-μm radiation were combined onto a common beam path by a dichroic mirror. A spherical lens with a focal length of 15 cm focused the laser radiation into the LiB$_3$O$_5$.
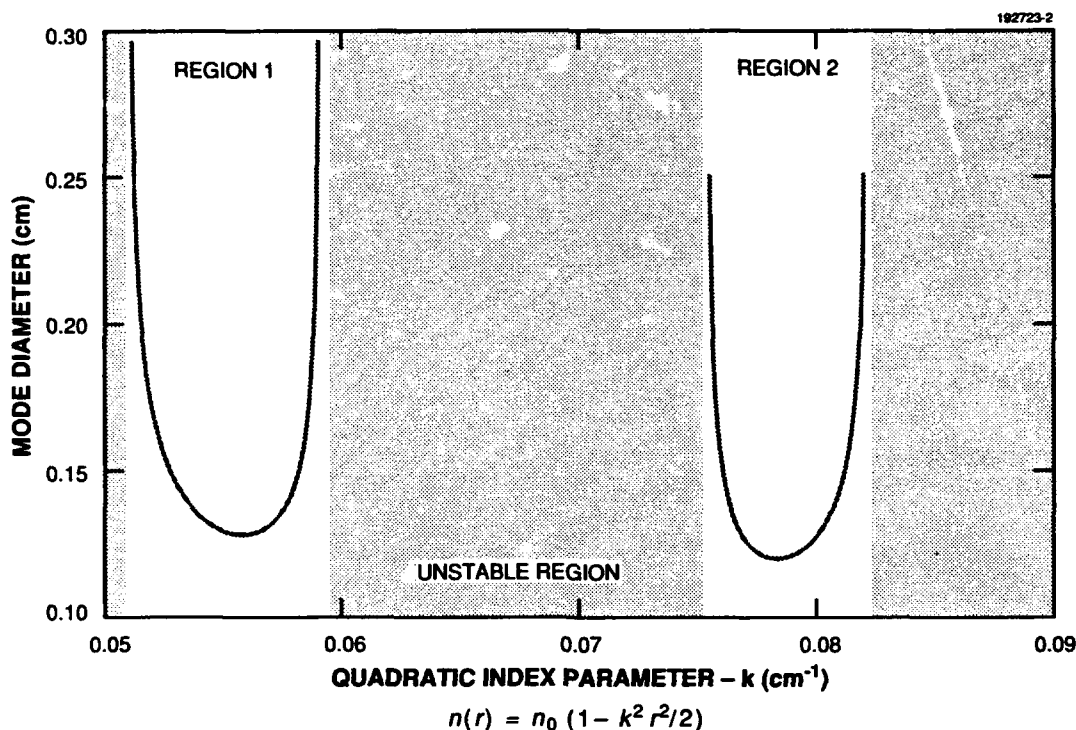
6

Figure 5. Calculated $1/e^2$ TEM$_{00}$ mode diameter in the 1.32-μm oscillator as a function of the Nd:YAG rod quadratic index parameter (k, in units of cm^{-1}). The mode diameter is taken halfway between the ends of the Nd:YAG rod. For the purpose of this calculation the 13.3-cm rods are placed symmetrically in the cavity with their faci͘g ends 20 cm apart and the other ends 41 cm from the flat cavity mirrors. Because the cavity is symmetric, the mode diameter is the same in both rods.

Typical long pulse operation of a Nd:YAG laser results in pronounced laser spiking or relaxation oscillations throughout the duration of the laser pulse. Laser spiking is caused by the development of laser gain that is greater than the steady state or threshold gain. The absence of appreciable stimulated emission at the start of laser pumping allows laser gain to rise substantially beyond threshold gain. This high initial gain leads to a rapid buildup in the laser radiation intensity, which then depletes the gain and after a short delay results in a greatly reduced radiation intensity. This low intensity and continued laser pumping allow the redevelopment of high laser gain and another intensity buildup. The cycle of low intensity/high gain followed by high intensity/low gain continues through the rest of the laser pulse with a damping rate dependent on the laser pumping rate and the laser cavity losses. In addition to the initial spiking, laser spiking behavior can be reexcited during the pulse by various cavity perturbations, such as acoustic noise.

Laser spiking can be suppressed by an intracavity nonlinear crystal, which converts high intensity laser spikes into second harmonic radiation [5]. Because the peak intensities of the initial laser spikes are substantially reduced through second harmonic generation, they do not drive the laser gain as far below threshold. Thus the laser spiking behavior damps out at a much higher rate than in the absence of intracavity doubling, and the redevelopment of spiking is suppressed. The rate of damping can be increased by raising the second
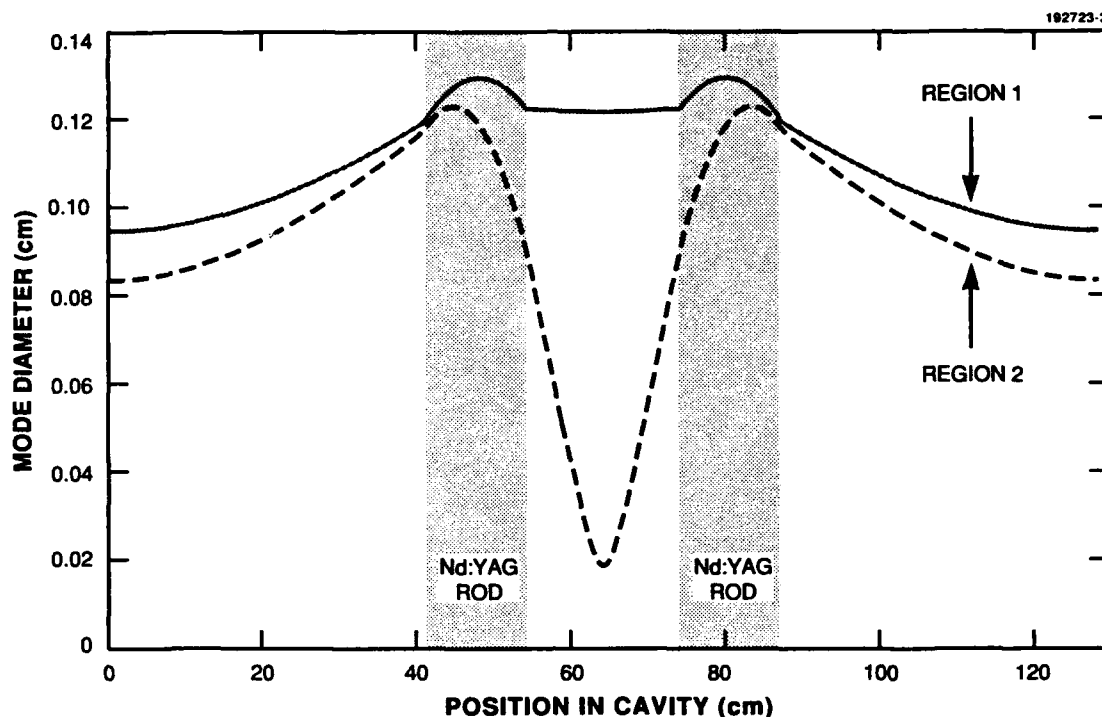
7

Figure 6. Calculated $1/e^2$ TEM_{00} mode diameter in the 1.32-μm oscillator as a function of position in the cavity. (The end mirrors are at 0 and 129 cm.) The upper and lower curves correspond to operation of the oscillator with a quadratic index parameter in the center of regions 1 (k = 0.055 cm^{-1}) and 2 (k = 0.0785 cm^{-1}), respectively (see Figure 5). For the purpose of this calculation the 13.3-cm rods are placed symmetrically in the cavity with their facing ends 20 cm apart and the other ends 41 cm from the flat cavity mirrors.

harmonic conversion efficiency: increase the intracavity radiation fluence through decreased output coupling, use a nonlinear crystal with a high nonlinear coefficient, and position it at an intracavity beam waist. Mode-locking also increases second harmonic generation. When mode-locked the peak power of the laser radiation increases, and second harmonic radiation is generated with greater efficiency.

It is important to eliminate the independent spiking behavior of the 1.06- and 1.32-μm lasers to obtain good temporal overlap of the laser pulses for efficient sum-frequency mixing; therefore, both the 1.06- and 1.32-μm laser cavities contain a nonlinear crystal to suppress laser spiking through second harmonic generation. The 1.06-μm oscillator contains a KTP crystal; because of its relatively large phase-matching angular acceptance, careful alignment of the crystal is not required. Unfortunately the KTP crystal absorbs enough 1.06- and 0.532-μm radiation to heat up during laser operation. This heating results in birefringence changes that must be compensated by an intracavity 1/4 waveplate to avoid a substantial reduction in laser power. The 1.32-μm laser cavity contains an $LiIO_3$ crystal because the KTP crystal, which was ordered for this purpose, was not properly cut for second harmonic generation of 1.32-μm radiation. Because $LiIO_3$ has a narrow phase-matching angular acceptance, careful alignment is required; however, this crystal is not substantially heated by laser radiation, and no adjustment of the intracavity 1/4 waveplate is required during laser operation.

8

Improved stability of both laser oscillators can probably be achieved by replacing the current intracavity crystals with angle-tuned and temperature-stabilized LiB_3O_5 crystals.

Typical temporal profiles of the 1.06- and 1.32-μm macropulses are shown in Figure 7. Each macropulse consists of a train of mode-locked micropulses spaced at 10-ns intervals. The 1.06-μm macropulse has an FWHM duration of $\approx$100 μs, while the 1.32-μm macropulse has an FWHM duration of $\approx$65 μs. The relaxation oscillations are not completely damped in either laser oscillator because complete damping causes the micropulses to have greater pulse widths and less peak intensity, which results in reduced efficiency for sum-frequency mixing.
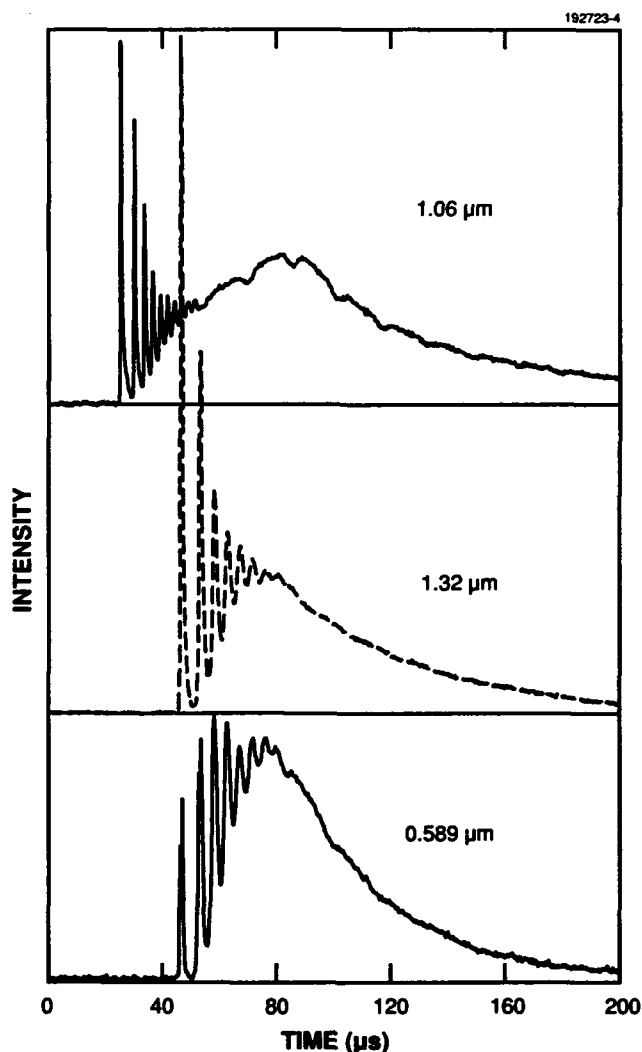

Figure 7. Macropulse temporal profiles for the 1.06- and 1.32-μm laser pulses and the 0.589-μm sum radiation. The detectors used in these measurements were not fast enough to sense the 100-MHz mode-locked pulse train within each macropulse.

9

Micropulses are generated by mode-locking the laser oscillators to achieve higher peak powers for efficient sum-frequency mixing. An acoustically resonant quartz crystal, which is piezoelectrically driven by an RF source at $\approx$50 MHz with about 3 W of power, is inserted into each oscillator for mode locking. By carefully adjusting the cavity lengths and longitudinal mode spacings, the lasers can be mode-locked at a micropulse repetition rate of $\approx$100 MHz. The mode-locked micropulse duration can be shortened by increasing the RF power to the quartz crystal by moving the crystal further from the output mirror (shortening the temporal window in which a micropulse must travel through the crystal, to the mirror, and back through the crystal without experiencing substantial loss) and by transversely translating the crystal. But short laser micropulses can only be obtained at the expense of laser power. The theoretical limit to the micropulse duration is controlled by the available gain bandwidth; however, a practical limit is imposed by the variation in the laser cavity length during a macropulse. The optical length of the laser cavity varies during the laser pulse because of thermal and excited-state-population transients that produce index-of-refraction transients in the Nd:YAG laser rods, resulting in a timing variation of good mode-locking during the laser macropulse for very short micropulses. By adjusting the laser cavity length, the timing of good mode-locking can be moved about in the macropulse. The shortest duration micropulses for which good mode-locking can be maintained over the full macropulse is about 300 ps.

The 1.06- and 1.32-μm laser mode-lockers are driven by a common frequency source to ensure phase-locked emission of the micropulses. By adjusting the relative phase of the drive signal to each mode-locker, the timing of the 1.06- and 1.32-μm micropulses can be adjusted for optimal temporal overlap in the sum-frequency mixing crystal. Typical temporal profiles of the laser micropulses are shown in Figure 8. The 1.06-μm micropulse has an FWHM duration of $\approx$350 ps, while the 1.32-μm micropulse has an FWHM duration of $\approx$500 ps.

Each oscillator contains a single, angle-tuned, solid etalon for wavelength control. The wavelength of the 1.32-μm laser is tuned for maximum 1.32-μm power. The 1.06-μm laser is then tuned so that the wavelength of the sum radiation is coincident with the sodium D_2 transition (0.5889973-μm air wavelength). The 1.32-μm laser is polarized by an intracavity Brewster plate, while the much higher small signal gain at 1.06 μm requires that this laser be polarized by an intracavity dielectric polarizer. The 1/4 waveplates on either side of the Nd:YAG rods in both oscillators allow compensation for the natural birefringence in the intracavity nonlinear crystal and the stress-induced birefringence in the mode-locker. The 1.32-μm oscillator also contains a dichroic mirror, having high reflectivity at 1.06 μm and high transmission at 1.32 μm to prohibit lasing at 1.06 μm (the 1.06-μm stimulated emission cross section is ~5 times greater than at 1.32 μm). The 1.06- and 1.32-μm laser oscillators have 60% and 40% output couplers with average polarized output powers of ~20 and ~12 W, respectively. Typical transverse beam profiles of the 1.06- and 1.32-μm laser oscillators are shown in Figures 9 and 10.

192723-5
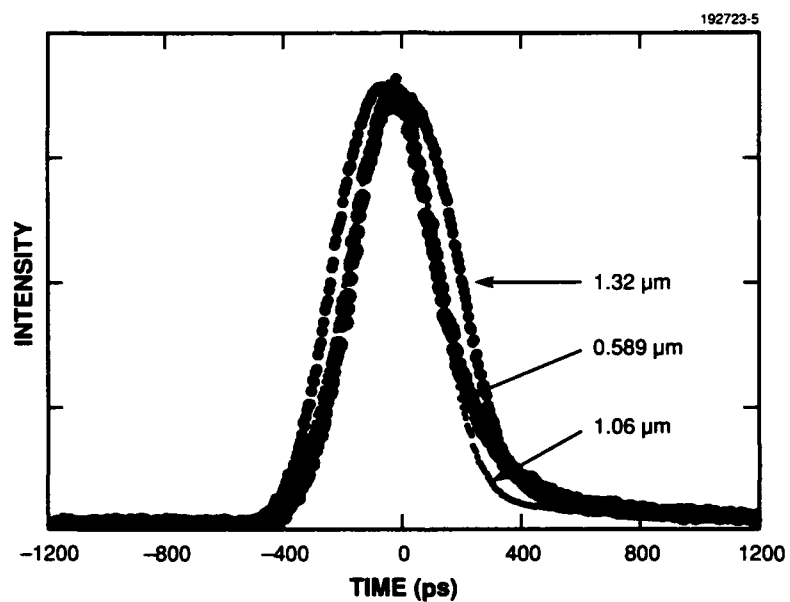
Figure 8. Micropulse temporal profiles for the 1.06- and 1.32-µm lasers and the 0.589-µm sum radiation. Note that the 1.06- and 1.32-µm 100-MHz mode-locked micropulses are not of equal width. More efficient sum-frequency generation can be achieved by making the micropulses of equal duration.

11

Figure 9. Spatial far-field transverse profile of the 1.06-µm laser oscillator beam.

Figure 10. Spatial far-field transverse profile of the 1.32-µm laser oscillator beam.

3. LASER AMPLIFIERS

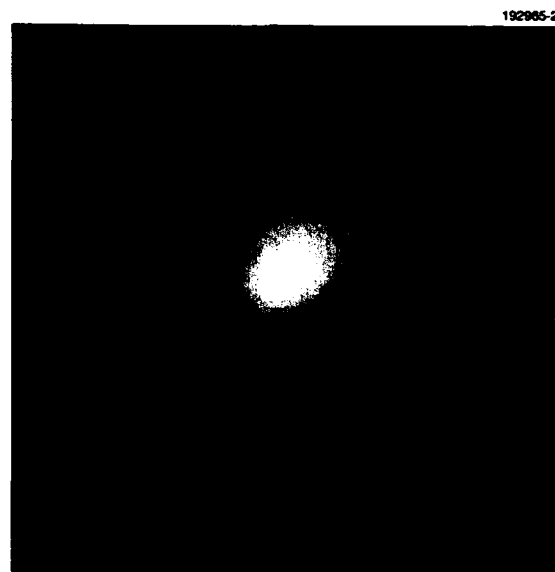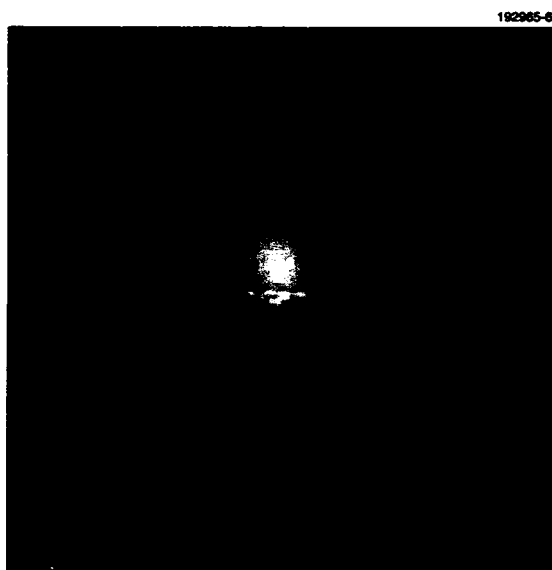Because the laser oscillators do not provide enough power for the sum-frequency generation of 20 W of sodium resonance radiation, it is necessary to pass the output of each oscillator through a pair of matched amplifiers that are configured so that the laser oscillator beam travels along the thermal center of the Nd:YAG amplifier rods. A 90° polarization rotator is placed between each Nd:YAG rod for birefringence compensation. The laser beam is aligned in the thermal center of the rods in the same way as the oscillator rods are aligned except that either 1.06- or 1.32-μm rather than HeNe laser radiation is used to view the isogyre pattern. This alignment is critical to obtain a well-polarized beam from the amplifiers with good transverse beam quality.

The 1.32-μm amplifiers are pumped at power levels similar to the oscillators and contain Nd:YAG rods identical to those of the oscillator. These amplifiers are optimized by placing them at a distance from the oscillator output coupler equal to the distance between the oscillator Nd:YAG rods and the output coupler. This geometry assures that the transverse laser beam characteristics are nearly the same in the amplifier as in the oscillator and that the laser beam travels through the second Nd:YAG amplifier rod symmetrically to the way that it travels through the first amplifier rod, resulting in optimum birefringence compensation.

The 14-mJ output of the 1.32-μm oscillator is passed through the amplifiers in a cross-sectional area of 0.013 cm^2; thus the fluence entering the amplifiers is 1.1 J/cm^2, which is below the saturation fluence of 3.4 J/cm^2. At the output of the amplifier the 1.32-μm beam has increased in intensity by a factor of 1.8 with a fluence of 2 J/cm^2. Because the amplifiers are operated at or below the saturation fluence, energy extraction from the amplifiers is not efficient.

Several attempts were made to double-pass the amplifiers to increase the energy extraction efficiency at 1.32-μm (see Figure 11); however, the strong birefringence of the amplifier rods caused enough laser beam depolarization after double-passing the amplifiers so that some of the laser energy passed back through the polarizer between the oscillator and the amplifier and caused unacceptable spectral and mode-locking instabilities. By placing a low-loss optical isolator between the oscillator and the amplifier, it should be possible to double-pass the amplifiers and obtain much better energy extraction. It currently appears that terbium gallium garnet would provide the best Faraday rotation material for a 1.32-μm optical isolator. The absorption coefficient of this material was measured to be 1.7×10^{-4} cm^{-1} at 1.32 μm.

The 1.32-μm amplifier output energy is 25 mJ per pulse. By carefully aligning the beam through the amplifiers, most of this energy is transmitted through a final polarizer with good beam quality. Figure 12 shows the transverse beam profile of the 1.32-μm laser beam after passing though the amplifiers and the polarizer. Without carefully aligning the 1.32-μm laser beam with the thermal center of the amplifier rods, the transverse profile and the sum-frequency mixing efficiency of this beam are severely degraded.

The 1.06-μm oscillator produces 24 mJ per pulse with a beam diameter of 0.85 mm. The amplifiers are positioned as far as possible from the oscillator output coupler to allow the 1.06-μm beam to expand and better fill the amplifiers. The 1.06-μm amplifier rods are 6 mm in diameter and 133 mm in length.
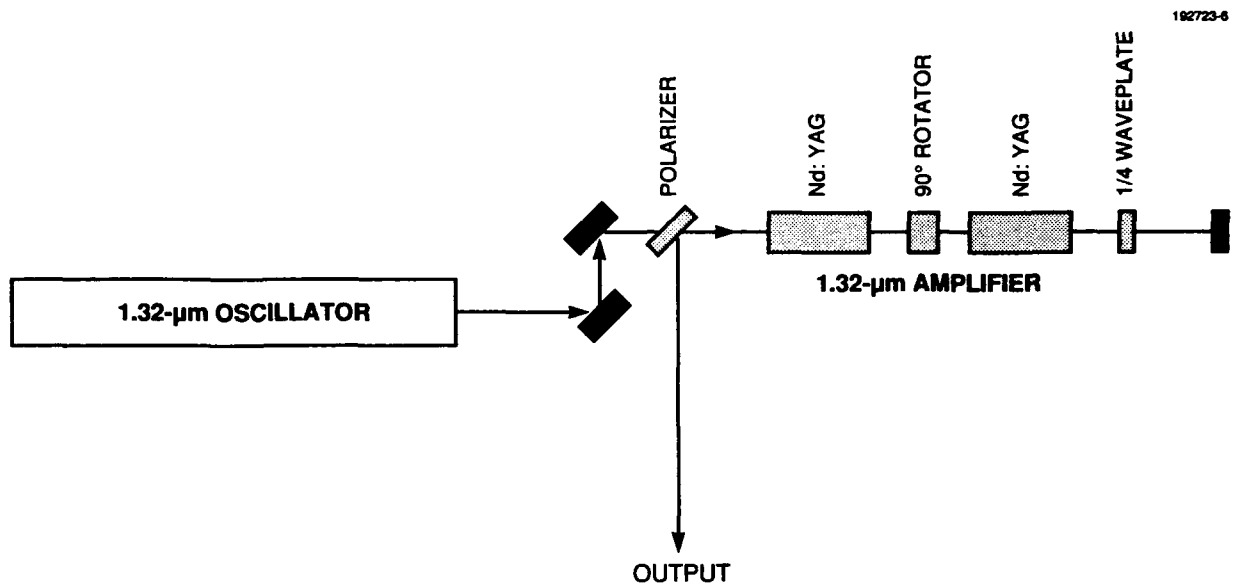
Figure 11. Double-pass amplifier schematic. Depolarization of the laser beam resulted in some 1.32-μm radiation passing through the polarizer and into the oscillator. This radiation caused the oscillator to operate very unstably. As a result, the double-pass geometry was not used in the final laser system sent to the Air Force Phillips Laboratory.

Figure 12. Spatial far-field transverse profile of the 1.32-μm laser beam after passing through the 1.32-μm amplifier.

14

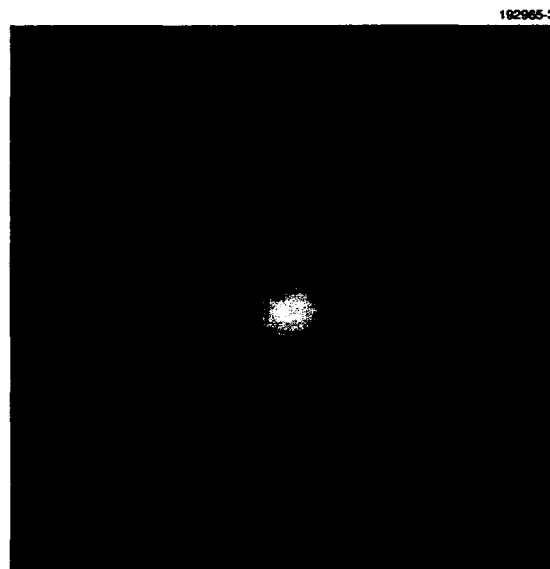The beam cross-sectional area in the amplifiers is about 5×10^{-2} cm^2, resulting in a fluence of about 0.48 J/cm^2, which is slightly less than the saturation fluence of 0.67 J/cm^2. At the output of the amplifier the 1.06-μm beam power has increased by a factor of 2.3 and has a fluence of 1.1 J/cm^2. Figure 13 shows the isogyre pattern of the 1.06-μm beam after passing through the amplifier and a crossed polarizer.

Figure 13. Spatial transverse profile of the 1.06-μm laser beam after passing through the 1.06-μm amplifier and a crossed polarizer. This represents a good isogyre profile.

15

4. SUM-FREQUENCY GENERATION OF SODIUM RESONANCE RADIATION

The utility of a nonlinear crystal for efficient sum-frequency mixing is determined not only by the nonlinear coefficients of the crystal but often, more importantly, by the phase matching and optical damage characteristics of the crystal. Severe constraints are placed on the nonlinear crystal during efficient mixing of low peak power radiation, which must be tightly focused into the crystal to achieve high peak intensities; the angular content of the focused radiation must be kept less than the phase-matching angular acceptance of the crystal. The relatively narrow angular acceptance of crystals such as KH_2PO_4, $LiIO_3$, and $KNbO_3$, limits the degree of focusing that can profitably be applied to the pump radiation.

If, in addition, the radiation is cw or is pulsed with a high duty cycle, then tight focusing results in a high average intensity at the focus, which can produce substantial local heating of the crystal if there is absorption of even a small fraction of either the incident or the sum-frequency radiation. Heating the crystal results in a local temperature gradient, which can adversely affect the sum-frequency mixing efficiency if the gradient exceeds the phase-matching temperature acceptance of the crystal or if the gradient results in mechanical stress to the crystal; such stress can affect the phase-matching process or result in physical damage to the crystal. High average intensities can result in photorefractive damage to the crystal. In particular the small temperature acceptance, relatively high optical absorption coefficients, and high susceptibility to photorefractive damage of crystals such as $LiNbO_3$ and $KNbO_3$, severely limit their utility in high average intensity applications. Table 1 lists the phase matching characteristics for frequency summing of 1.06- and 1.32-μm radiation in several nonlinear crystals [6–9].

Because the 840-Hz laser system generates relatively low peak intensity, radiation must be tightly focused into the nonlinear crystal to achieve peak intensities consistent with efficient mixing. Tight focusing results in a relatively large range of angles in which radiation propagates. The first three crystals listed in Table 1 ($LiIO_3$, β-BaB_2O_4, and $KNbO_3$) have very small phase-matching angular acceptance and cannot be used with the 840-Hz laser system.

$LiNbO_3$, KTP, and LiB_3O_5 each have relatively large angular acceptances; especially $LiNbO_3$ and LiB_3O_5, which can be noncritically phase matched. While $LiNbO_3$ has the largest figure of merit of these three crystals, it has the lowest physical damage threshold and is subject to photorefractive damage [10] below the annealing temperature of 200°C. Noncritical phase matching of 1.06-, 1.32-, and 0.589-μm radiation in $LiNbO_3$ occurs at 225°C. Because the phase-matching temperature acceptance is very low, $LiNbO_3$ must be housed in a temperature-controlled oven. At high average powers temperature gradients across the crystal cross section, caused by absorption of the fundamental and sum radiation, can substantially limit the maximum possible sum-frequency mixing efficiency. Previous mixing in noncritically phase-matched $LiNbO_3$ resulted in the generation of 300 mW of average power sodium resonance radiation without any evidence of photorefractive damage [11]; however, when $LiNbO_3$ was used to mix the 1.06- and 1.32-μm radiation from the 840-Hz laser system, severe photorefractive effects limited the amount of sum radiation that could be generated (with good beam quality) to less than 1 W. As much

as 5-W sum radiation was ultimately generated in $LiNbO_3$; however, its beam quality was very poor. Photorefractive damage was observed at 225°C, which is, to the writers' knowledge, the highest crystal temperature at which such damage has been observed in $LiNbO_3$.

TABLE 1
Phase-Matching Characteristics

Material	Type of Phase Matching	d_{eff} (pm/V)	Figure of Merit (pm/V)^2	Walkoff Angle (deg)	FWHM Acceptance		
					Angular (mrad — cm)	Spectral$^\nabla$ (Å — cm)	Thermal$^\nabla$ (°C — cm)
$LiIO_3$	I	1.9[a1]	0.54	3.9	0.4	5.2	(Large)
β-BaB_2O_4	I	2.1[a1]	1	3	0.6	58	55
$KNbO_3$[c]	I	13.9[a2]	17.7	3.4	0.4	1.2	0.3
KD*P	II[b]	0.4[a1]	0.004	1.5	2	55	7
KD*P	III[b]	0.3[a1]	0.0025	1.1	3.3		
KTP[d]	II	2.9[a1]	1.5	2.5	1.5	5.6	25
KTP[d]	III	3.2[a1]	1.8	1.3	3.2		
$LiNbO_3$[e]	I	5.9[a3]	3.2	0	40		0.35[g]
LiB_3O_5[f]	I	1.24[a4]	0.38	0	50		6[g]

$^\nabla$1.06-μm SHG values (for reference only).

(a1–4) Based on nonlinear coefficient values given in References [6–9], respectively.

(b) Type II — 1.32- and 0.589-μm polarizations parallel; Type III — 1.06- and 0.589-μm polarizations parallel.

(c) Beams directed in bc plane.

(d) Beams directed in xz plane.

(e) Noncritical temperature phase matched; T = 227 °C, θ = 90°.

(f) Noncritical temperature phase matched; T = 41 °C, θ = 90°, ϕ = 0°.

(g) Sum generation values.

It was previously shown that adverse thermal and photorefractive effects in harmonic generation in $KNbO_3$ could be dramatically reduced by using a revolving beam geometry that distributes the thermal and photorefractive load over a large crystal volume [12]. Figure 14 is a schematic of the revolving beam geometry for harmonic generation (or sum-frequency mixing). Input radiation passes through a polarizer and then reflects off a mirror that is spinning about an axis slightly off normal to the mirror surface. After being reflected from the mirror the radiation travels along a path on the surface of a cone until it is refracted by

a lens that is placed one focal length from the spinning mirror. The radiation then travels along the surface of a cylinder and passes through the nonlinear crystal. The harmonic (sum-frequency) radiation generated in the crystal is reflected by a dichroic mirror back through the crystal and lens to the spinning mirror. After reflection from the spinning mirror the beam of harmonic (sum-frequency) radiation is stationary. This radiation travels backward along the direction of the incoming fundamental radiation. Because the harmonic (sum-frequency) radiation is polarized at right angles to the fundamental radiation it is rejected by the polarizer. A photograph of second harmonic generation in $KNbO_3$ with a revolving beam geometry is shown in Figure 15. An image of the harmonic radiation at the nonlinear crystal is shown in Figure 16. Because the fundamental radiation was pulsed at 5.18 kHz while the mirror was spun at 140 Hz, 37 different crystal positions produced harmonic radiation. The improvement in second harmonic beam quality resulting from revolving the fundamental beam in the nonlinear crystal is shown in Figure 17; the transverse beam profiles were taken after the harmonic radiation had been rejected by the polarizer.

In an attempt to substantially reduce the photorefractive damage in $LiNbO_3$ caused by the high average power of the 840-Hz laser system, a revolving beam sum-frequency mixing geometry was constructed. Figure 18 shows the 1-cm diameter × 5-cm-long $LiNbO_3$ crystal and its oven. Unfortunately at high average input power this crystal was damaged (see Figure 19), illustrating a disadvantage of the revolving beam geometry. By using a larger volume and surface area of the nonlinear crystal, its damage threshold is reduced to that of the weakest part of the crystal. If the rotation rate of the mirror is not a subharmonic of the laser repetition rate, then a single point of damage will propagate around the circle that the input radiation describes.
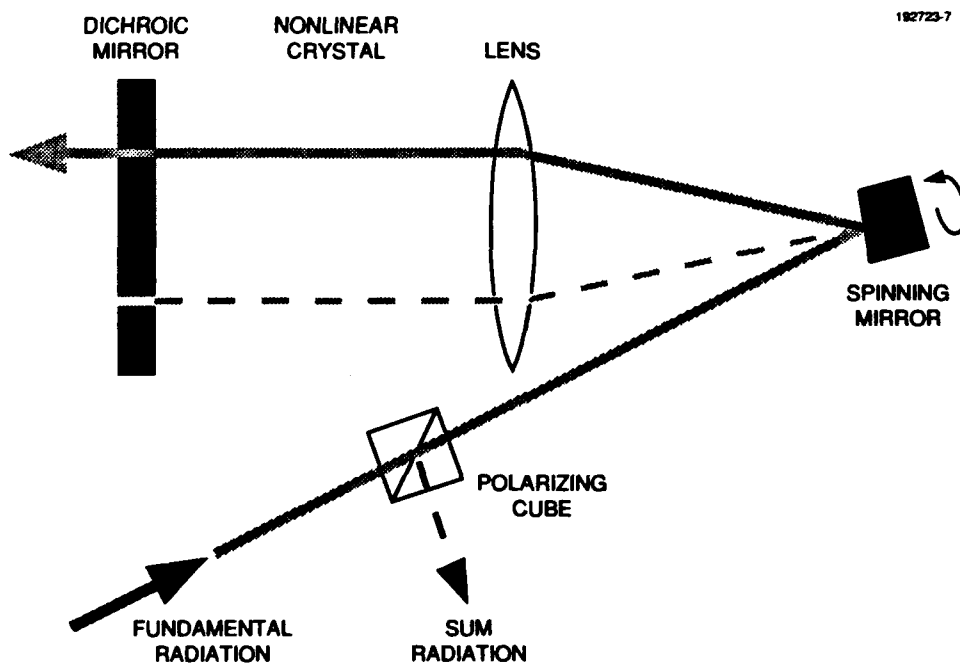

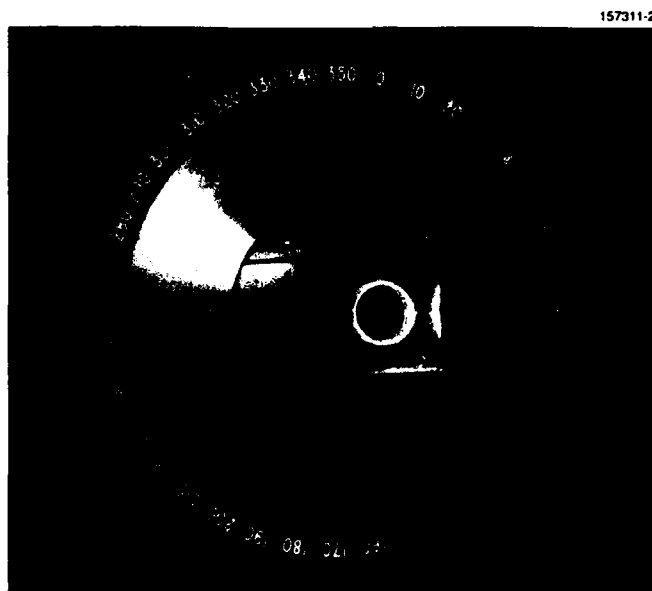Figure 14. Schematic of revolving beam geometry for either second harmonic generation or sum-frequency mixing.

157311-2

Figure 15. Photograph of KNbO$_3$ crystal in which the revolving beam geometry has been used for second harmonic generation of 0.532-µm radiation.

157311-1

Figure 16. Photograph of the image of the KNbO$_3$ crystal in which the revolving-beam geometry has been used. The 37 discrete spots are a result of the fact that the laser repetition rate was 37 times the rotation rate of the spinning mirror.
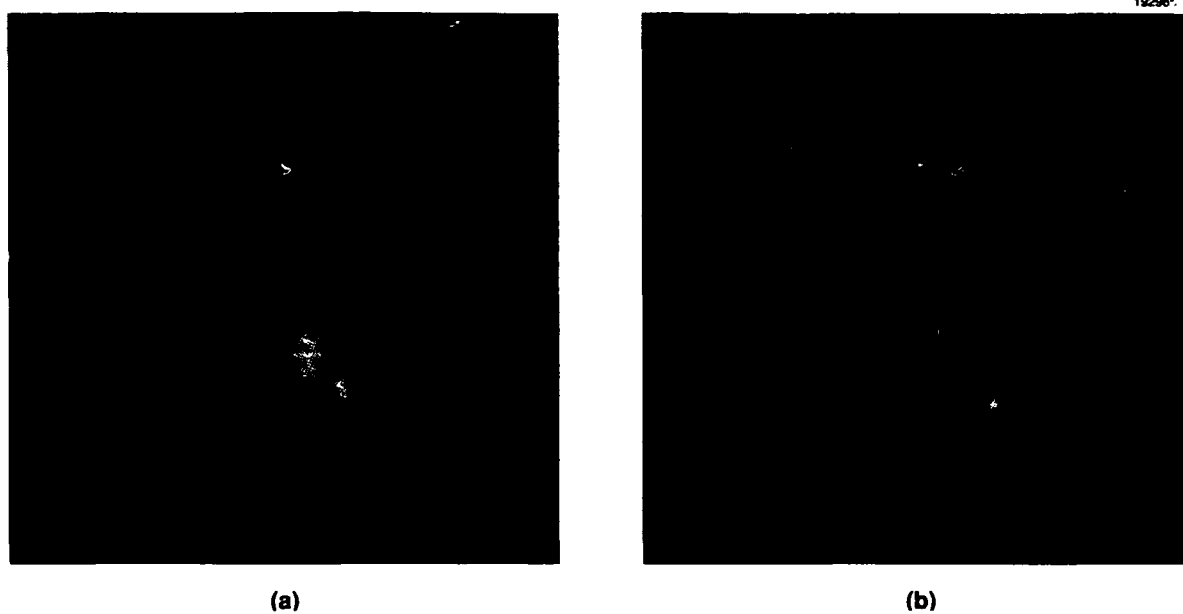
20

(a)

(b)

Figure 17. Transverse spatial beam profiles of the second harmonic radiation for an (a) revolving and a (b) stationary fundamental beam.

Figure 18. Photograph of the LiNbO₃ crystal and oven that were used in a revolving beam sum-frequency mixing
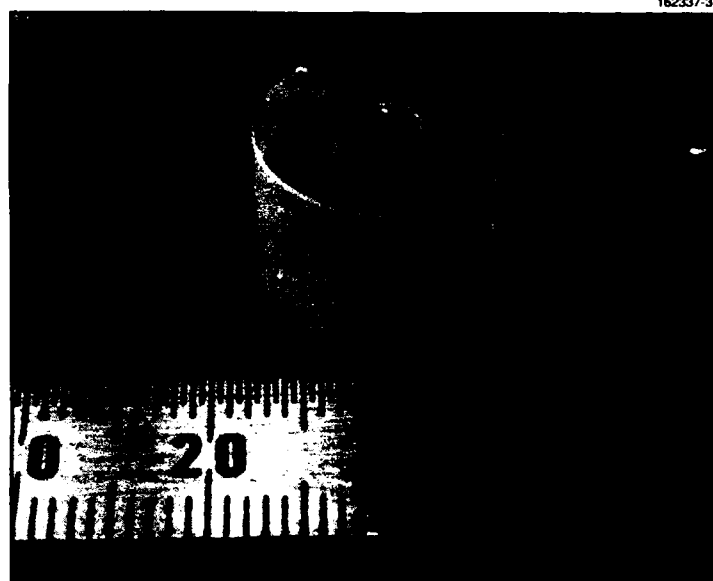
21

Figure 19. Photograph of the damage sustained by the $LiNbO_3$ crystal when used in the revolving beam geometry.

The arc of surface damage shown in Figure 19 was caused by the propagation of an initially small point of damage. This disadvantage of the revolving beam geometry can be overcome by forcing the mirror rotation rate to be a subharmonic of the laser repetition rate and by dividing the nonlinear crystal into several crystals; damage to one will not propagate to those adjacent.

KTP is much less susceptible to both photorefractive and physical damage than $LiNbO_3$. By using a 1.5-cm-long KTP crystal, as much as 3-W sum radiation has been generated with the 840-Hz laser system; however, at this power level there was evidence of degradation of the sum radiation beam quality. This degradation is believed to have resulted from absorption of radiation in the KTP crystal, causing thermally induced distortions in the laser beam.

LiB_3O_5 has recently become commercially available. This nonlinear material has several advantages for efficient mixing of low peak power, high duty cycle Nd:YAG laser radiation. By temperature tuning the crystal may be noncritically phase matched and, therefore, has a very large phase matching angular acceptance; however, contrary to other temperature tunable crystals, LiB_3O_5 retains a relatively large phase-matching temperature acceptance [13]. The relative mixing efficiency of LiB_3O_5 as a function of temperature is shown in Figure 20. Its most interesting characteristic for high average intensity applications is its low optical absorption coefficients of 1.2×10^{-3} cm^{-1}, 1.8×10^{-3} cm^{-1}, and 1.7×10^{-3} cm^{-1} at 1.32, 1.06, and 0.589 μm, respectively [14]. Lower optical absorption results in smaller thermal gradients and contributes to the high damage threshold of LiB_3O_5. These characteristics also allow tight focusing of high duty cycle radiation into LiB_3O_5.
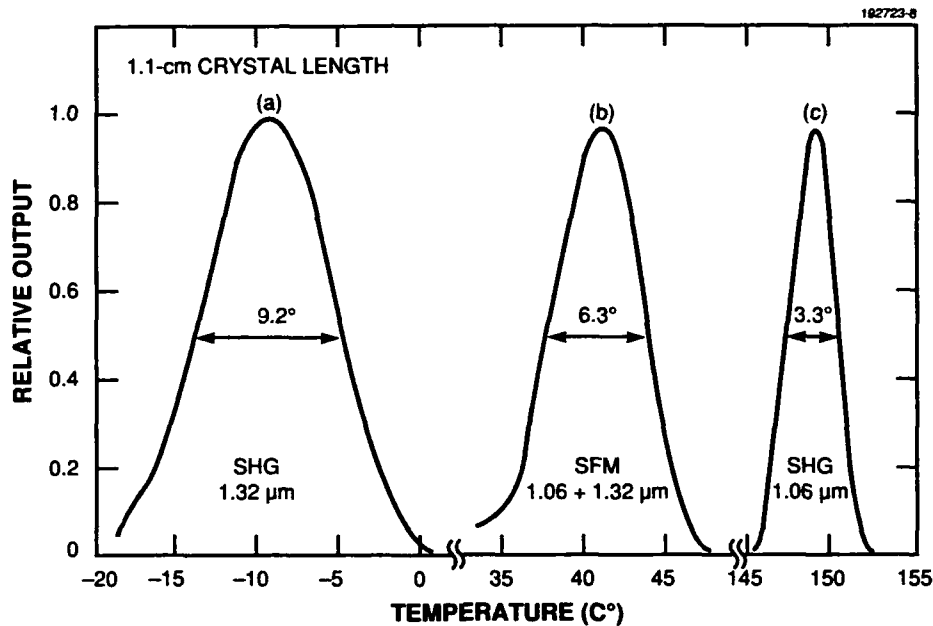
22

Figure 20. Noncritically phase-matched temperature tuning in an LiB₃O₅ crystal with radiation directed along the 1.1-cm-long crystal X-axis for (a) frequency doubling 1.32 µm, (b) frequency summing 1.06 and 1.32 µm, and (c) frequency doubling 1.06 µm.

After passing through the amplifiers, the 1.06- and 1.32-μm laser beams are combined with a dichroic mirror and then focused by a 15-cm focal length lens to a ~50-μm diameter (FWHM) spot in a 2- × 3.5- × 18.2-mm LiB$_3$O$_5$ crystal (x-cut, $\theta = 90°$, $\phi = 0°$). Tighter focusing of the incident laser beams was not beneficial even though the experimentally determined optimum beam diameter was three times larger than the calculated optimum for second harmonic generation [15]. The nonlinear crystal is oriented for Type I noncritical phase matching, which is achieved by heating the crystal to a temperature of 41°C. The radiation propagates parallel to the long dimension of the crystal.

By focusing 46 and 20 W of 1.06- and 1.32-μm radiation, respectively, into the LiB$_3$O$_5$ crystal, 20 W of 589-nm radiation has been generated. A photograph of the LiB$_3$O$_5$ housing is shown in Figure 21. The maximum measured external power conversion efficiency is 30%. At the focus the crystal is subjected to greater than 1 MW/cm^2 of average intensity. The external sum-frequency mixing power and efficiency as a function of total input power is shown in Figure 22. Because the LiB$_3$O$_5$ crystal is not antireflection coated, 5% of the fundamental and the sum radiation is lost to reflections at the crystal faces. Accounting for this loss yields an average internal mixing efficiency of 33%. In addition the 1.06- and 1.32-μm macropulses are not of equal duration as shown in Figure 7. A lower limit on the peak mixing efficiency can be estimated by multiplying the average internal mixing efficiency by the ratio of the 1.32- and 1.06-μm pulse durations. This yields a peak mixing efficiency of 50%. No photorefractive or physical damage is observed under these conditions. The transverse beam quality of the 0.589-μm radiation is shown in Figure 23.

23

Figure 21. Photograph of the LiB₃O₅ housing showing the generation of sum-frequency radiation. The 1.06- and 1.32-μm radiation go into the crystal from the right and the sum radiation exits to the left. The weak beam of sum radiation on the right is a result of a 5% reflection off the uncoated left side of the LiB₃O₅ crystal.

Using the oscillators alone, the sum-frequency mixing efficiency as a function of total input power is shown in Figure 24. While confined to lower sum-frequency powers than the oscillator-amplifier system, a laser system composed of oscillators only would probably deliver its maximum sum-frequency power more reliably.
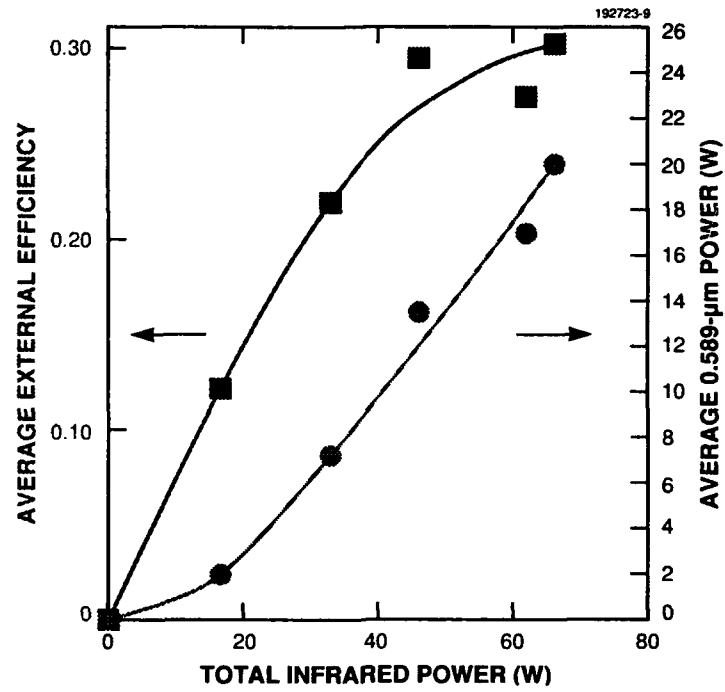
24

Figure 22. Average power and mixing efficiency of sodium resonance radiation as a function of the total infrared power coming from both the 1.06- and 1.32-μm amplifiers.
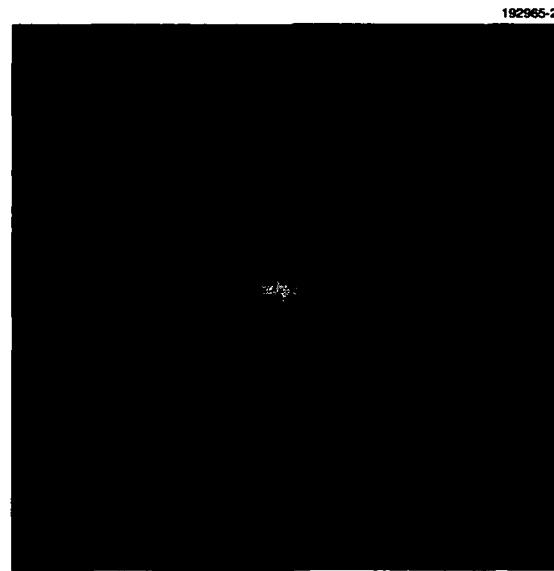

Figure 23. Spatial far-field transverse profile of the 0.589-μm radiation exiting from the LiB_3O_5 crystal.
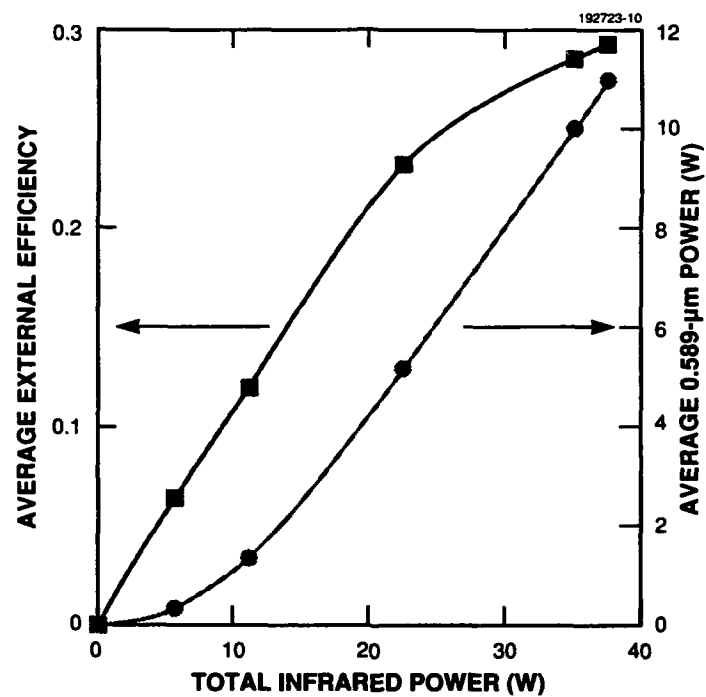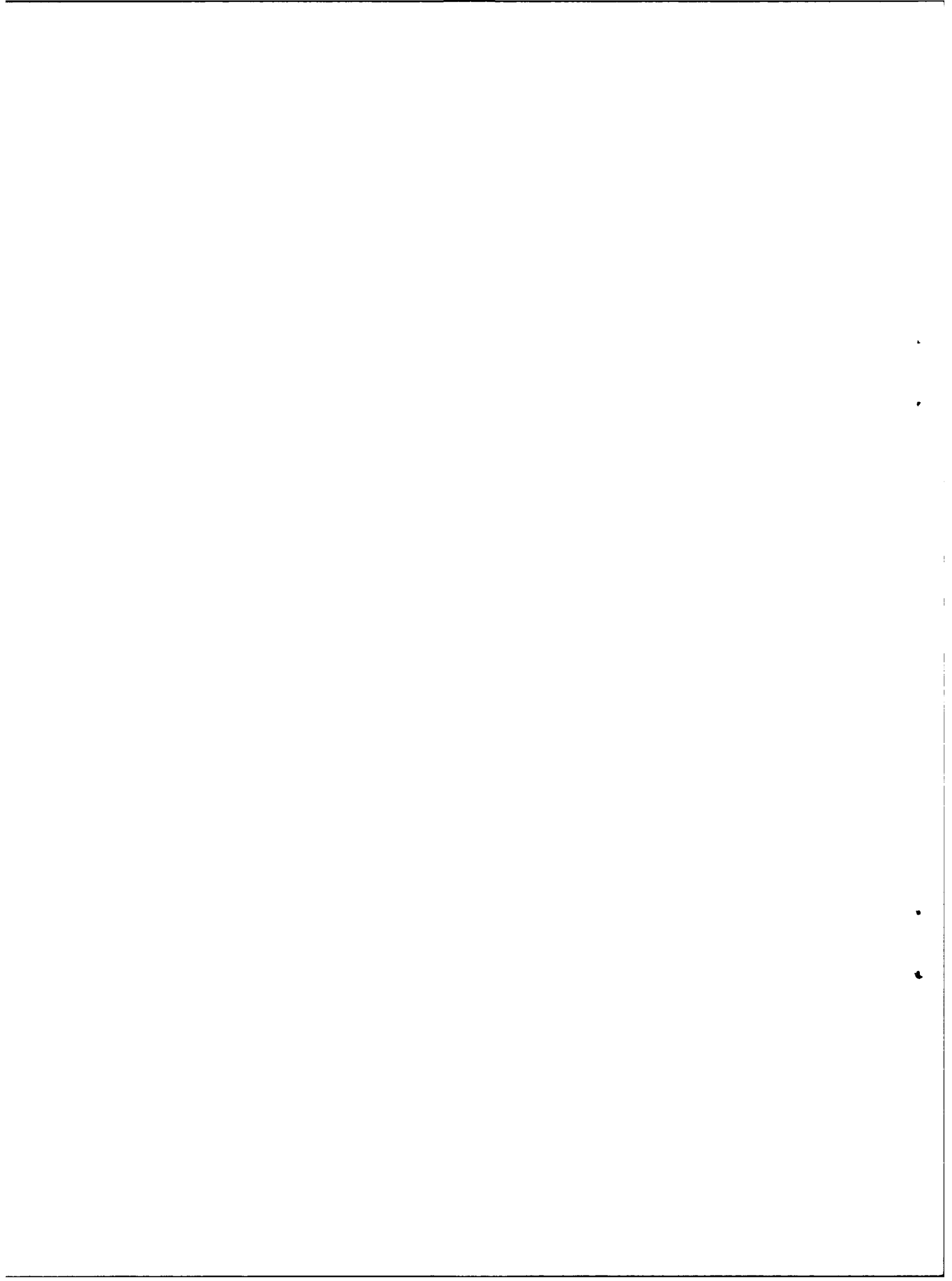
Figure 24. Average power and mixing efficiency of sodium resonance radiation as a function of the total infrared power coming from only the 1.06- and 1.32-µm oscillators.

5. SUMMARY

A 20-W laser source of sodium resonance radiation has been developed and delivered to the Air Force Phillips Laboratory. Sodium resonance radiation was generated with 30% average external mixing efficiency of the Nd:YAG laser radiation in a crystal of LiB_3O_5. This crystal withstood an average intensity of greater than 1 MW/cm^2 without optical or photorefractive damage. KTP and $LiNbO_3$ have been investigated for this application of sum-frequency mixing and found to be inferior to LiB_3O_5. The concept of using revolving beams to lower the fluence in a nonlinear crystal has also been tested.

REFERENCES

1. W. Koechner, *Solid-State Laser Engineering* 2nd ed., N.Y.: Springer-Verlag (1988), p. 358.

2. Ibid. p. 362.

3. W.C. Scott and M. deWitt, "Birefringence compensation and TEM_{00} mode enchancement in a Nd:YAG laser," *Appl. Phys. Lett.* **18**, 3 (1971).

4. W. Koechner, *Solid-State Laser Engineering* 2nd ed., N.Y.: Springer-Verlag (1988), p. 366.

5. T.H. Jeys, "Suppression of laser spiking by intracavity second harmonic generation," *Appl. Opt.* **30**, 1011 (1991).

6. R.C. Eckardt, H. Masuda, Y.X. Fan, and R.L. Byer, "Absolute and relative nonlinear optical coefficients of KDP, KD*P, BaB_2O_4, $LiIO_3$, $MgO:LiNbO_3$, and KTP measured by phase-matched second harmonic generation," *IEEE J. Quantum Electron,* **26**, 922 (1990).

7. J.C. Baumert, J. Hoffnagle, and P. Günter, "Nonlinear optical effects in $KNbO_3$ crystals at $Al_xGa_{1-x}As$, dye, ruby and Nd:YAG laser wavelengths," *SPIE* **492**, 374 (1984).

8. M.M. Choy and R.L. Byer, "Accurate second-order susceptibility measurements of visible and infrared nonlinear crystals," *Phys. Rev.* **B14**, 1693 (1976).

9. C. Chen, Y. Wu, A. Jiang, B. Wu, G. You, R. Li, and S. Lin, "New nonlinear-optical crystal: LiB_3O_5," *J. Opt. Soc. Am.* **B16**, 16 (1989).

10. A.M. Glass, "The photorefractive effect," *Opt. Eng.* **17**, 470 (1978).

11. T.H. Jeys, A.A. Brailove, A. Mooradian, "Sum frequency generation of sodium resonance radiation," *Appl. Opt.* **28**, 2588 (1989).

12. V. Daneu, T.H. Jeys, and J. Korn, "Mechanical beam scanning for optical mixing in nonlinear crystals," Lexington, Mass.: MIT Lincoln Laboratory, Solid State Research Report (1990:1).

13. N. Menyuk and J. Korn, "Thermal and absorptive properties of LiB_3O_5," Lexington, Mass.: MIT Lincoln Laboratory, Solid State Research Report (1990:1).

14. Ibid.

15. G.D. Boyd and D.A. Kleinman, "Parametric interaction of focused Gaussian light beams," *J. App. Phys.* **39**, 3597 (1968).

REPORT DOCUMENTATION PAGE

Public reporting burden for this collection of information is estimated to average 1 hour per response, including the time for reviewing instructions, searching existing data sources, gathering and maintaining the data needed, and completing and reviewing the collection of information. Send comments regarding this burden estimate or any other aspect of this collection of information, including suggestions for reducing this burden, to Washington Headquarters Services, Directorate for Information Operations and Reports, 1215 Jefferson Davis Highway, Suite 1204, Arlington, VA 22202-4302, and to the Office of Management and Budget, Paperwork Reduction Project (0704-0188), Washington, DC 20503.

1. AGENCY USE ONLY (*Leave blank*)	2. REPORT DATE 11 May 1992	3. REPORT TYPE AND DATES COVERED Final Report: January 1989 – March 1991

4. TITLE AND SUBTITLE

840-Hz Nd:YAG Laser Source of Sodium Resonance Radiation

6. AUTHOR(S)

Thomas H. Jeys, Kevin F. Wall, and Jeffrey Korn

5. FUNDING NUMBERS

C — F19628-90-C-0002
PE — 63605F
PR — 268

7. PERFORMING ORGANIZATION NAME(S) AND ADDRESS(ES)

Lincoln Laboratory, MIT
P.O. Box 73
Lexington, MA 02173-9108

8. PERFORMING ORGANIZATION REPORT NUMBER

TR-928

9. SPONSORING/MONITORING AGENCY NAME(S) AND ADDRESS(ES)

Air Force Phillips Laboratory
Kirtland Air Force Base, NM 87110

10. SPONSORING/MONITORING AGENCY REPORT NUMBER

ESD-TR-91-187

11. SUPPLEMENTARY NOTES

None

12a. DISTRIBUTION/AVAILABILITY STATEMENT

Approved for public release; distribution is unlimited.

12b. DISTRIBUTION CODE

13. ABSTRACT (*Maximum 200 words*)

A 20-W average power laser source of sodium resonance radiation has been developed and delivered to the Air Force Phillips Laboratory to generate a fluorescence spot in the earth's mesospheric sodium layer for atmospheric adaptive optics applications. The sodium resonance radiation was generated by sum-frequency mixing 1.06- and 1.32-μm Nd:YAG laser radiation in a lithium triborate crystal. The pulsed Nd:YAG lasers operated with a repetition rate of 840 Hz and pulse lengths of about 100 μs. The sum radiation was resonant with the sodium D_2 transition and generated with an average mixing efficiency of 30%. The lasers were mode-locked with a controlled pulse width that provided a spectrally broadened output matched to the 3-GHz Doppler-broadened absorption width of mesospheric sodium.

14. SUBJECT TERMS

Nd: YAG lasers   sodium resonance radiation
sum-frequency mixing   mesospheric sodium
lithium triborate   adaptive optics

15. NUMBER OF PAGES
40

16. PRICE CODE

17. SECURITY CLASSIFICATION OF REPORT Unclassified	18. SECURITY CLASSIFICATION OF THIS PAGE Unclassified	19. SECURITY CLASSIFICATION OF ABSTRACT Unclassified	20. LIMITATION OF ABSTRACT SAR